

JGR Space Physics

RESEARCH ARTICLE

10.1029/2023JA032171

Key Points:

- The model well reproduces lowaltitude electron data by considering azimuthal drift, pitch angle diffusion, and atmospheric backscatter
- Five POES/MetOp satellites are used to constrain model parameter evolution and quantify pitch angle diffusion rates
- Precipitation is identified as the dominant loss mechanism for electrons in the energy range 300–850 keV during the event of our study

Supporting Information:

Supporting Information may be found in the online version of this article.

Correspondence to:

Z.-G. Li, zhigu.li@mail.wvu.edu

Citation:

Li, Z.-G., Tu, W., Selesnick, R., & Huang, J. (2024). Modeling the contribution of precipitation loss to a radiation belt electron dropout observed by Van Allen Probes. *Journal of Geophysical Research: Space Physics*, 129, e2023JA032171. https://doi.org/10.1029/2023JA032171

Received 12 OCT 2023 Accepted 25 FEB 2024

Modeling the Contribution of Precipitation Loss to a Radiation Belt Electron Dropout Observed by Van Allen Probes

Zhi-Gu Li¹, Weichao Tu¹, Richard Selesnick², and Jinbei Huang¹

¹Department of Physics and Astronomy, West Virginia University, Morgantown, WV, USA, ²Space Vehicles Directorate, Air Force Research Laboratory, Kirtland AFB, NM, USA

Abstract A drift-diffusion model is used to simulate the low-altitude electron distribution, accounting for azimuthal drift, pitch angle diffusion, and atmospheric backscattering effects during a rapid electron dropout event on 21st August 2013, at L=4.5. Additional external loss effects are introduced during times when the low-altitude electron distribution cannot be reproduced by diffusion alone. The model utilizes low-altitude electron count rate data from five POES/MetOp satellites to quantify pitch angle diffusion rates. Low-altitude data provides critical constraint on the model because it includes the drift loss cone region where the electron distribution in longitude is highly dependent on the balance between azimuthal drift and pitch angle diffusion. Furthermore, a newly derived angular response function for the detectors onboard POES/MetOp is employed to accurately incorporate the bounce loss cone measurements, which have been previously contaminated by electrons from outside the nominal field-of-view. While constrained by low-altitude data, the model also shows reasonable agreement with high-altitude data. Pitch angle diffusion rates during the event are quantified and are faster at lower energies. Precipitation is determined to account for all of the total loss observed for 450 keV electrons, 88% for 600 keV and 38% for 900 keV. Predictions made in the MeV range are deemed unreliable as the integral energy channels E3 and P6 fail to provide the necessary constraint at relativistic energies.

1. Introduction

The dynamics of the outer terrestrial radiation belt can be exceedingly variable and is instigated ultimately by solar activity. The population of the outer belt is dominated by energetic (>0.5 MeV) electrons and extends from approximately 3 to 7 Earth radii (R_E) (Ganushkina et al., 2011; Van Allen et al., 1958). The presence of these MeV electrons heavily influences the operations of near-Earth satellites and can cause catastrophic damage as they penetrate deep into sensitive electronics (Baker, 2000). Furthermore, energetic electrons which precipitate from the radiation belts into the Earth's atmosphere have been found to increase production of nitrogen oxides (NO_x), leading to rapid depletion of the ozone layer (e.g., Fytterer et al., 2015; Meraner & Schmidt, 2018), and enhanced ionospheric conductance (e.g., Robinson et al., 1987; Yu et al., 2018).

It has been well known, especially recently with data from the Van Allen Probes (VAP), that relativistic electron flux within the radiation belts can decrease rapidly on orders of magnitudes within only a few hours (see e.g., Baker et al., 2016; Shprits et al., 2012). However, the mechanisms responsible for these so-called rapid electron dropout events are not well understood. Magnetopause shadowing in combination with radial diffusion provides an efficient mechanism responsible for fast electron loss, as they funnel previously trapped electrons toward the magnetopause where they are subsequently lost traversing open field lines (see e.g., X. Li et al., 1997; Shprits, Thorne, et al., 2006; Tu et al., 2019; Turner et al., 2012). However, at the heart of outer radiation belts ($L \approx 4$), it is believed that precipitation of electrons onto the terrestrial atmosphere via pitch angle diffusion serves as the dominant mechanism responsible for electron dropouts (Millan et al., 2010; Selesnick, 2006; Turner et al., 2014). The pitch angles of trapped electrons can eventually be scattered into the loss cone, a range of pitch angles with mirror points within the dense atmosphere, where they then subsequently precipitate.

Early attempts to quantify pitch angle diffusion rates were made by Kennel and Petschek (1966), Thorne and Kennel (1971), and Lyons et al. (1972). However, without comprehensive information about the wave's spectral properties, cold plasma densities, or ion composition, these estimates were hampered by uncertainties and broad assumptions. Currently, estimated electron loss rates from pitch angle scattering still diverge greatly. For example, Shprits et al. (2005) employed electron lifetimes in their model of 10 days within the plasmasphere and

© 2024. American Geophysical Union. All Rights Reserved.

LI ET AL.



0.7-4 days outside the plasmasphere, depending on the K_p index. Comparatively, Barker et al. (2005) used a L dependent electron lifetime ranging from 3 days at L=6-29 days at L=4. Modeling work done by Tu et al. (2010) estimated relativistic electron lifetimes to vary from 0.01 to 10 days during magnetic storm events. These conflicting estimates underscore the persisting ambiguity surrounding pitch angle diffusion rates and their driving mechanisms. Accurate quantification of electron pitch angle diffusion and loss rates would be of value as they are ubiquitous in comprehensive radiation belt models and are also needed to reliably assess electron acceleration processes.

Theoretically, the non-dipolar nature of the terrestrial magnetic field causes nonuniform electron loss in magnetic longitude, where the resulting redistribution due to azimuthal drift provides the necessary low-altitude observational constraint to infer pitch angle diffusion rates. This approach was validated by Imhof (1968) where an approximate analytical solution to the diffusion equation showed reasonable agreement with data from lowaltitude satellites. Detailed simulations were done by Abel and Thorne (1999) further confirming the significant role of both pitch angle diffusion and azimuthal drift in the loss of radiation belt electrons, but however, was not compared to observational data. Subsequently, Selesnick et al. (2003) developed a parametric model, accounting for azimuthal drift and pitch angle diffusion, and used low-altitude SAMPEX satellite data to constrain the rate of pitch angle diffusion within the model. The model was capable of predicting temporal and spatial variation of pitch angle diffusion without the need for global wave measurements, which led to multiple subsequent works (including this one, see also e.g., Selesnick, 2006; Tu et al., 2010). However, the temporal resolution provided by the model is significantly reduced by the limited availability of data from just one satellite, enabling a cadence as low as only half a day. Magnetospheric conditions during storm time can vary much more rapidly, leading to misleading results, or missing storm-time dynamics. This issue was addressed by Pham et al. (2017) by using an extensive set of low-altitude data obtained from a more recent satellite constellation composed of Polar Orbiting Environmental Satellites (POES) operated by the National Oceanic and Atmospheric Administration (NOAA) and the Meteorological Operational Satellites (MetOp) operated by the European Organization for the Exploitation of Meteorological Satellites (EUMETSAT). Five POES/MetOp satellites were online during their event study, which provided their model with an improved 3-hr cadence.

An accurate angular response function for detectors is required under weak pitch angle diffusion, where the loss cone is relatively empty. This is because trapped electron flux outside of the loss cone are typically several orders-of-magnitude higher, where any measurements taken inside the loss cone are dominated by the trapped electrons outside of the field-of-view (FOV). While the bounce-averaged models used in Pham et al. (2017) and preceding works are capable in approximating the loss cone flux under both weak and strong diffusion scenarios, there did not exist any reliable loss cone measurements to constrain the model evolution in such regions. Consequently, their models assumed an empty loss cone, and so their results were valid in only the weak diffusion limit. Selesnick et al. (2020) derived a more accurate angular response function for the detectors onboard POES/MetOp, accounting for the response to particles from all incident angles. By incorporating this new angular response function, POES/MetOp's loss cone measurements can provide a more accurate constrain for model flux inside the loss cone region.

In this work, we use an updated drift-diffusion model to dynamically simulate the distribution of low-altitude electrons and quantify the pitch angle diffusion rates during a rapid electron dropout event at L = 4.5 on 21st August 2013. The newly derived angular response function is used in combination with the previously established energy response function (Yando et al., 2011) to convert the simulated electron distribution function to count rates which are then compared to the observed count rates from POES/MetOp. The model includes the dominant effects of pitch angle diffusion and azimuthal drift as experienced by energetic low-altitude electrons and, in addition, atmospheric backscattering effects of electrons within the loss cone. The model parameters, including pitch angle diffusion rates, are determined by fitting simulated POES/MetOp count rate data to observations. Notably, this approach does not rely on wave measurements. Its results could potentially be used to constrain the distribution of waves that are responsible for the precipitation loss, though we do not attempt that here. Furthermore, with the availability of VAP data, additional insight on the model results can be obtained by comparisons with high-altitude data, which was not done in previous works related to this model. Section 2 provides an overview of low-altitude electron data and their significance in determining pitch angle diffusion rates. Section 3 details the model, including the initial conditions obtained from VAP, while Section 4 describes the dropout event. Section 5 presents the model results followed finally by comparisons with high-altitude data, conclusion, and further discussions in Sections 6 and 7 respectively.

LI ET AL. 2 of 16



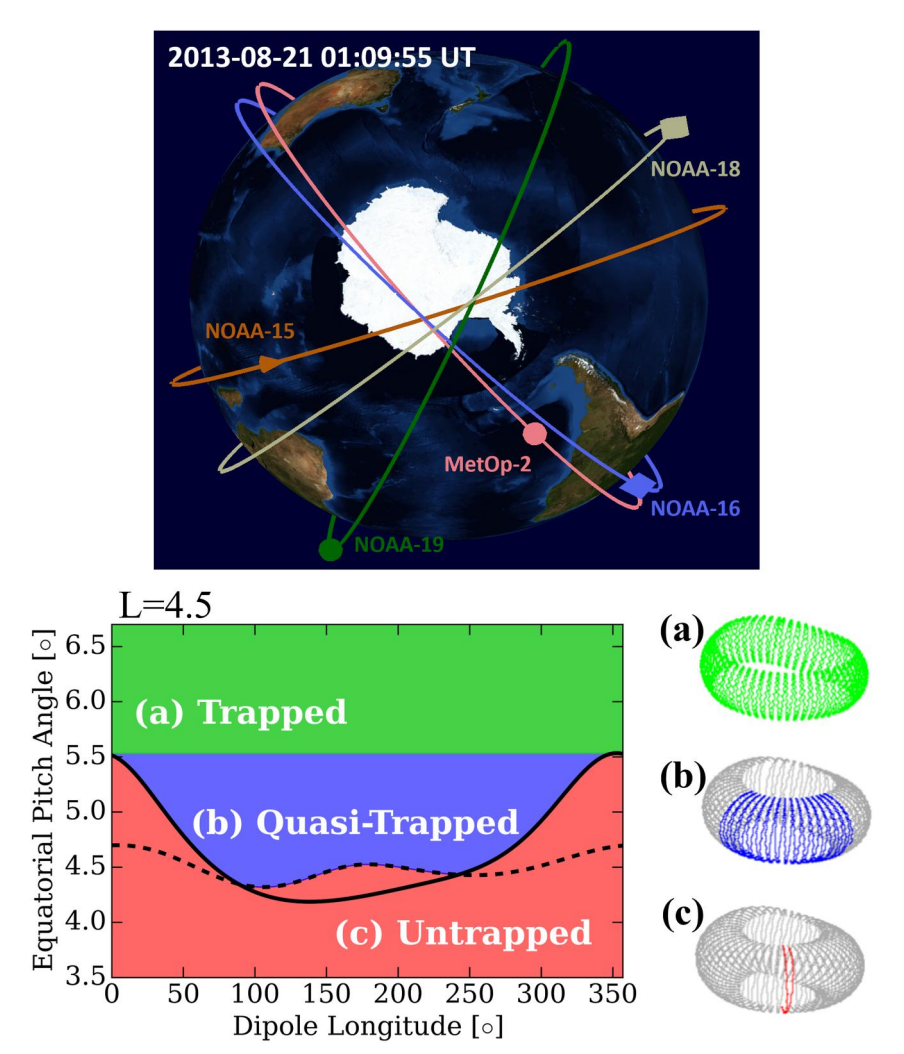


Figure 1. Top panel shows the orbits of five POES/MetOp satellites on 21 August 2013, viewed from above Antarctica. Bottom left panel shows the partitioned regions of trapped, quasi-trapped, and untrapped electrons based on their equatorial pitch angles at L = 4.5. The dashed and solid black line represents the northern and southern hemisphere bounce loss cones respectively. The highlighted path on the bottom right tori exemplifies the trajectories of a particle in each category. Bottom panels are adapted from Tu et al. (2010).

2. Low-Altitude Electron and Trapping Regions

The distribution of electrons mirroring near and within the upper boundary of the terrestrial atmosphere can be categorized into three distinct groups. Aside from electrons that mirror well above or deeply within the atmosphere, which are categorized as the *trapped* and *untrapped* electron populations, due to non-dipolar nature of the terrestrial magnetic field, there arises an intermediate category called the *quasi-trapped*, where particles can mirror above or within the atmosphere depending on their location in magnetic longitude. This is because, near the surface, the higher-order magnetic multipoles asymmetrically determine the elevation of the particle's mirror point in relation to the 100 km altitude threshold—upper boundary layer of the Earth's atmosphere.

Figure 1, bottom left panel, shows the variation of equatorial north (dashed curve) and south (solid curve) loss cones calculated at 100 km altitude versus dipole longitude at a constant McIlwain L-shell value (hereinafter referred to as L, see e.g., McIlwain, 1961). The dipole longitude (hereinafter referred to as longitude) increases in the same direction as electron drift and is measured from the intersection between the dipole equator with the geographic prime meridian. The particle will attempt to mirror across both hemispheres, so therefore, the larger of the two angles at each longitude governs whether a particle will mirror below the atmosphere within a single bounce period. This is known as the bounce loss cone (BLC, red region in Figure 1) and the untrapped electron

LI ET AL. 3 of 16



population pertains equatorial pitch angles below the BLC curve, since it is likely that they precipitate within a singular bounce.

Extending this idea, the quasi-trapped population of electrons exists with certain pitch angles who mirror above the atmosphere at their local longitude but eventually drift into the BLC at another longitude and precipitate. Consequently, most of these electrons are lost near $\sim 300^{\circ}$ longitude to the southern loss cone. This results in enhanced electron precipitation over the south Atlantic and is known as the South Atlantic Anomaly (SAA). The region in momentum space populated by the quasi-trapped electrons constitutes the drift loss cone (DLC, blue region in Figure 1), where the boundaries are defined by the maximum value of the BLC in longitude and the BLC itself. Lastly for completeness, the previously mentioned trapped population (green region in Figure 1) are those outside of the DLC and therefore remain trapped within the radiation belts indefinitely.

The distribution of electrons within these three categories serves as a good constraint on the rate of pitch angle scattering and electron loss rate within the radiation belts. Count rate data of the low-altitude electrons are obtained from the Medium Energy Proton and Electron Detector (MEPED) which is a part of the Space Environment Monitor 2 (SEM-2) instrument suite (Evans & Greer, 2000). SEM-2/MEPED is flown onboard POES/MetOp. These satellites are in a Sun-synchronous polar orbit at an approximate altitude and period of 800 km and 1.7 hr respectively. Figure 1, top panel, shows the orbits of the five POES/MetOp satellites operational during the 21 August 2013, event, with level 2 (16 s averaged count rates) data available. The combination of Earth's rotation with the spread in local-time of these five satellites provides good coverage of all geographic longitudes within ~3 hr.

The MEPED detector is described in detail by Evans and Greer (2000). Its entrance aperture has a 15° half-angle nominal field of view (FOV) to incoming particles. Local pitch angles are derived from the IGRF magnetic field model since POES/MetOp does not carry a magnetometer onboard (Green, 2013). The electron telescope measuring count rate contains a single silicon detector and three integral energy channels labeled E1, E2, E3 corresponding to energies >30, >100, and >300 keV respectively. The proton telescope contains two silicon detectors and six integral energy channels P1−P6 with defined energy ranges. Additionally, P6 can serve as an electron channel, responding to electrons ≥700 keV when proton intensities are not too high (Yando et al., 2011). For our interests in energetic electron dropouts, E3 and P6 will be of interest to us for this study as they correspond more closely to radiation belt electron energies. Contamination from protons when using P6 as an electron channel can be an issue, however proton intensities are typically low in the outer belt. Furthermore, proton intensities are verified to be low during this particular event via P5 which is insensitive to electrons (Green, 2013).

The nominal values of energy response and FOV can serve as a good indicator of which electron population POES/MetOp are surveying. However, Selesnick et al. (2020) demonstrated that E3 and, in particular, P6 data can be dominated by electrons from outside the nominal FOV. Our model thus uses the more comprehensive energy and angular response functions provided by Yando et al. (2011) and Selesnick et al. (2020) respectively and the details can be found therein.

The MEPED detector onboard POES/MetOp has two telescopes oriented in orthogonal directions. At mid to higher latitudes (or equivalently $L \gtrsim 1.5$, since orbital altitude is constant), one of the telescopes points in a more magnetic field-aligned direction, while the other points perpendicular to the magnetic field. These have been appropriately named as the 0° and 90° telescope respectively. At these altitudes, the local BLC and DLC drastically widen, giving POES/MetOp an increased ability to distinguish between trapped, quasi-trapped and untrapped electron populations. Generally, the 90° telescope measures quasi-trapped electrons inside the DLC, except for near the SAA where it occasionally measures trapped electrons, while the 0° measures exclusively untrapped electrons deep inside the BLC. As an example, Figure 2a shows the pitch angle measurements made by five POES/MetOp satellites interpolated to L=4.5 over a 3-hr interval needed for sufficient longitudinal coverage. The local pitch angle measured is assumed to be from the center of the FOV and is mapped to the equator using IGRF-11 (Finlay et al., 2010). As stated earlier and seen in Figure 2a, the 90° telescope has excellent coverage of the quasi-trapped population in longitude with the occasional measurement of the trapped population, while on the other hand, the 0° telescope exclusively measures the untrapped electrons.

Figures 2a and 2b are correlated plots in the sense that they visualize the same 3-dimensional data but on two separate y-axes. Notably, each count rate point taken from the E3 channel presented on Figure 2b corresponds to a unique point on Figure 2a, indicating the associated pitch angle at the same longitude of the measurement. The

LI ET AL. 4 of 16

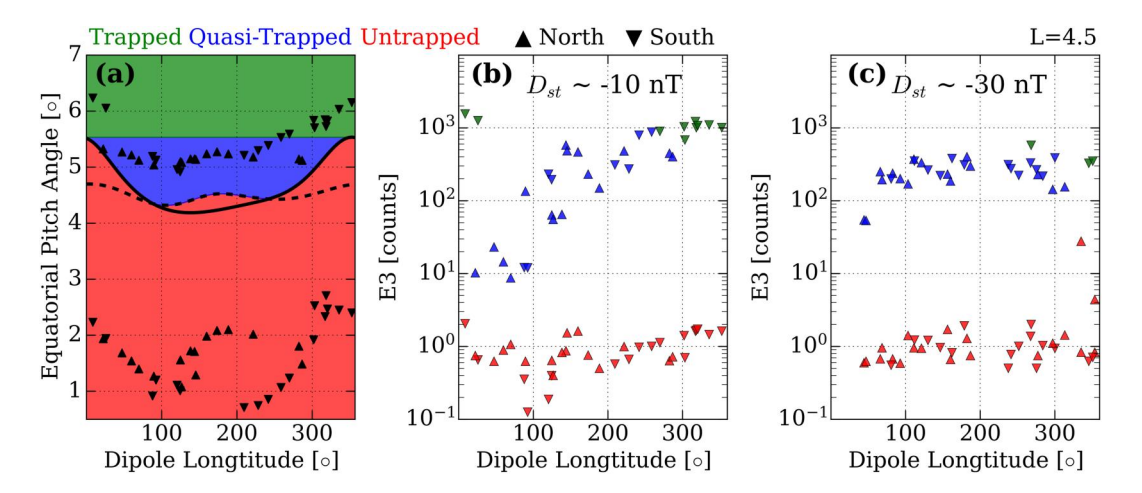


Figure 2. Panels (a) and (b) show equatorial pitch angle and E3 channel count rate measurements taken by POES/MetOp over a 3-hr period starting from 2013-08-21/00:00:00 UT. The upper and lower cluster of points on panel (a) are taken by the 90° and 0° telescope respectively. Panel (c) is taken over a 3-hr period starting from 2013-08-21/06:00:00 UT at a lower D_{ex} level.

minimum value of the Disturbance storm-time ($D_{\rm st}$) index over the 3-hr interval is -10 nT, suggesting low levels of pitch angle scattering, and this is reflected in the distribution of quasi-trapped count rates in longitude. The quasi-trapped population is derived from trapped electrons whose pitch angles have been scattered into the DLC. Hence, if the pitch angle scattering rate is comparable to the azimuthal drift speed of the electrons, the quasi-trapped flux should increase gradually as they drift toward larger longitudes. Subsequently, the increased quasi-trapped flux decreases as the electrons precipitate over the SAA which means the quasi-trapped count rates should attain its minimum near the region immediately after. This pattern of steady increase and sudden decrease within the DLC is manifested by a strong gradient of increase in the quasi-trapped count rates (blue triangles) in longitude as seen in Figure 2b. Trapped count rates (green triangles) are generally higher because they do not undergo periodic losses every drift orbit, while the untrapped count rates (red triangles) are nominally the lowest.

Figure 2c panel is in the same style as Figure 2b except its equatorial pitch angle measurements are not shown, and the data is taken at a different 3-hr interval with a minimum $D_{\rm st}$ value of $-30\,{\rm nT}$. In this case and with reference to Figure 2b, the scattering rate is increased while azimuthal drift speed remains the same. When scattering rates dominate the drift speed, the shape of the quasi-trapped count rate distribution loses its longitudinal dependance as shown in Figure 2c and the quasi-trapped count rate values become comparable to the trapped over all longitudes. Moreover, the shape of the quasi-trapped distribution becomes relatively insensitive to further increases in pitch angle scattering rates. However, even higher rates of pitch angle scattering can still be inferred by the precipitation models provided the additional constraints from the untrapped measurements.

3. Model Description

3.1. Drift-Diffusion Model

Selesnick et al. (2003) demonstrated that the primary characteristics of the electron's phase space density (f) at low altitudes are governed by the azimuthal drift motion and pitch angle diffusion due to wave-particle interactions. Additionally, the effects of scattering and loss due to atmospheric interactions for electrons mirroring within the atmosphere can be approximated by strong pitch angle diffusion and rapid decay respectively which was found to work well in reproducing the loss cone electron measurements made by POES/MetOp's 0° telescope (Selesnick et al., 2020). All together, these main contributing effects to the electron dynamics at a particular L and energy can be described by the bounce-averaged model

$$\frac{\partial f}{\partial t} + \omega_d \frac{\partial f}{\partial \phi} = \frac{1}{xT(y)} \frac{\partial}{\partial x} \left(xT(y) D_{xx} \frac{\partial f}{\partial x} \right) - \frac{4}{\tau_b} (1 - F_b) \Theta(x_c - x) f + \frac{\partial f}{\partial t} \bigg|_{\text{ext.}}, \tag{1}$$

where $f = f(x, \phi, t)$ is the electron phase space density as a function of magnetic longitude ϕ , time t, and $x = \cos \alpha_0$; α_0 is the equatorial pitch angle of the electron. ω_d and τ_b are the azimuthal drift frequency and bounce period of the

LI ET AL. 5 of 16



electron evaluated under a dipole approximation. The T(y) function is proportional to the electron bounce period and is approximated in a dipole field by $T(y) = 1.380173 - 0.639693y^{0.737}$, where $y = \sin{(\alpha_0)}$ (Davidson, 1976). x_c is the local (in ϕ) x value of the BLC. The BLC angle is determined by the maximum value between the loss cones in each hemisphere and is calculated using the IGRF-11 geomagnetic field model. Θ is the Heavyside step function which ensures that only electrons mirroring inside the atmosphere experiences atmospheric effects.

The advection term accounts for the eastwards azimuthal motion of the electrons due to gradient-curvature drift in the positive longitude direction (Roederer, 1970, p. 27). The x diffusion term accounts for the wave-particle interactions that stochastically scatters the particles from their original pitch angles (Schulz & Lanzerotti, 1974, p. 77). The decay term (Equation 1 second term on the right) captures the loss of electrons through momentum-degrading collisions with atmospheric particles where the decay rate is controlled by F_b , the ratio of electrons that are not lost but scattered back out of the atmosphere. Lastly, the third term on the right of Equation 1 accounts for source or loss due to any other external mechanisms (e.g., local heating or magnetopause shadowing). It is assumed to be the form

$$\frac{\partial f}{\partial t}\Big|_{\text{ext}} = \left(S_0 \tilde{E}^{-\nu} - L_0 \tilde{E}^{-\eta}\right) \frac{g_1(x,\phi)}{p^2},\tag{2}$$

where S_0 and L_0 (not to be confused with the McIlwain L shell parameter) are the external electron source and loss rates and are strictly positive. ν and η controls the energy dependance of these source and loss rates. S_0 , L_0 , ν , and η are free parameters to be determined by model fits to the low-altitude electron data. \tilde{E} is the particle energy normalized by 1 MeV and the electron's momentum squared p^2 is included in the denominator so that S_0 and L_0 have dimensions of intensity per unit time. g_1 is approximately the normalized first order eigenfunction of the drift-diffusion operator, derived numerically for when Equation 1 exhibited steady decay in absence of external source/loss. This was chosen because all higher order terms of source/loss decay more rapidly and therefore are not well constrained by data. Furthermore, the functional form of g_1 helps reduce any artificial diffusion for when source/loss is introduced. Since the source and loss function is not well constrained, it is only turned on as a last resort if the model cannot reproduce the observed data via pitch angle diffusion alone.

Selesnick (2006), Tu et al. (2010), and Pham et al. (2017) all used a functional dependence of $D_{xx} \sim x^{-\sigma}$ with a similar drift-diffusion model and reported reasonably good agreements between model and low-altitude data. We chose a D_{xx} of the form

$$D_{xx} = \frac{\tilde{E}^{-\mu} D_w}{10^{-4} + x^{20}} + D_b \Theta(x_c - x), \tag{3}$$

where we have found $\sigma=20$ to work well with our event study. D_w includes all pitch angle diffusion through various wave-particle interactions and μ serves as the energy dependance of the diffusion activity. Both D_w and μ are free parameters determined by model fits to the low-altitude data. The factor of 10^{-4} solely serves to maintain numerical stability at low x (higher α_0) values. The form of this first term in Equation 3 results in high diffusion for equatorial particles thus evolves f into a "flat-top" distribution (consistent with the VAP observations of electrons with energies between 100s keV and ~ 2 MeV during the event's storm time and will be discussed in Section 4). At low pitch angles, Equation 3 approaches $D_w \tilde{E}^{-\mu}$ which will largely determine the electron loss rate (Shprits, Li, & Thorne, 2006).

 F_b is a simplified description of the backscattered electrons that undergo mirroring below 100 km altitude and subsequently re-emerge from the atmosphere. The random scattering in pitch-angle due to atmospheric collisions is capture in D_b of Equation 3 as a diffusive process. The Θ Heavyside function ensures that this diffusive mechanism is limited to only the electrons within the BLC. F_b and D_b together dictates that the BLC electrons will undergo scattering of their pitch angle, and rapid decay due to momentum degrading collisions. The energy loss of the backscattering process is neglected since Selesnick et al. (2004) found the rate energy change per emergence out of the atmosphere is much less than the rate of decay itself. In our model, $F_b = 0.1/\tilde{E}$ is assumed, where the energy dependence is a simplified approximation based on the findings in Selesnick et al. (2004). The combination of F_b with $D_b = 10^{-7}$ s⁻¹ for all energies is found to match well with BLC electron measurements.

LI ET AL. 6 of 16



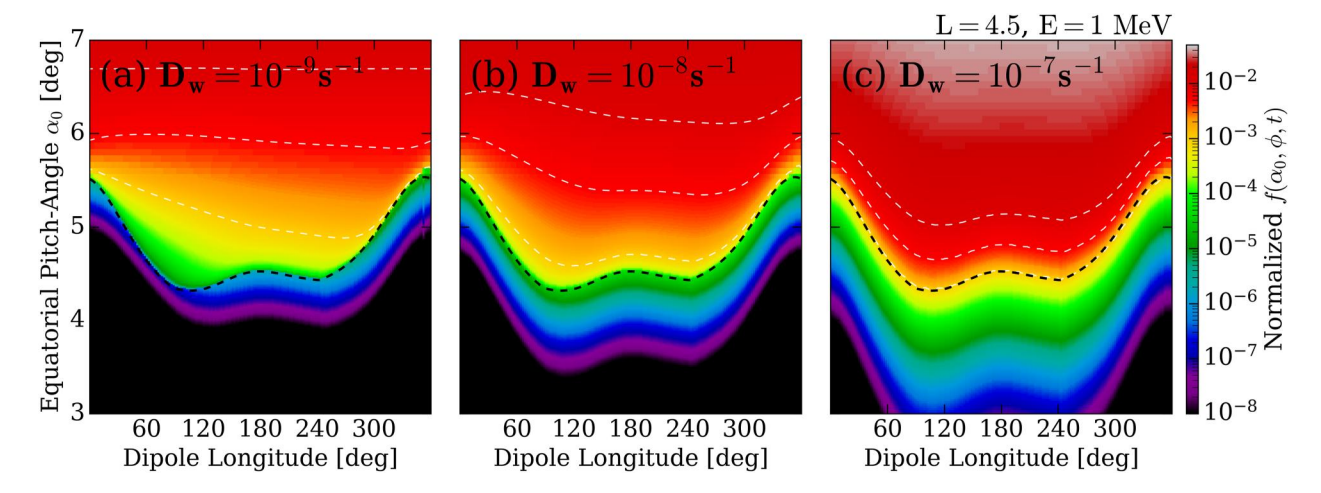


Figure 3. Example model solutions for a select value of energy and *L* with varying levels of pitch-angle diffusion. The color intensity plot is a normalized solution, and the dashed black line is the angle of the BLC. The dashed white lines are contours of the normalized *f*. The external source/loss term is turned off here.

Equation 1 is solved numerically at energies from 300 to 1,800 keV, spaced by 50 keV, using operator splitting to combine Crank-Nicholson method in x with first-order upwind scheme in ϕ (Press et al., 2007, p. 1048). The boundary conditions in x are $\partial f/\partial x = 0$ at x = 0, and x = 1. This would dictate no flow of electron currents in or out of the unphysical regions in x (or α_0). Periodic boundary conditions are applied in ϕ such that $f(\phi) = f(\phi + 2\pi)$.

Figure 3 shows sample solutions to Equation 1 with increasing levels of pitch angle diffusion. Here, $\mu=0$ so the diffusion coefficient becomes $D_{xx}=D_w$ at the low pitch angles near the DLC. From Figure 3, it is evident that the distributions of electrons at low altitudes are strongly dependent on the diffusion rates or, more specifically, the ratio D_{xx}/ω_d . In the case of Figure 3a, the distribution of electrons at the lower altitudes is azimuthal drift dominated where the slow rate of pitch angle diffusion does not fill in the DLC at all longitudes. Furthermore, the solution above the DLC is largely unaffected by the shape of the BLC (shown by the lack of ϕ dependence in the white contour lines). Conversely, Figure 3c demonstrates a case where diffusion dominates. Here, the effect of azimuthal drift becomes largely irrelevant and the local solution at each longitude is primarily dictated by its pitch angle relative to the local BLC. Consequently, lines of constant f tightly hugs the BLC at all longitudes. The solutions of f above the DLC becomes more longitudinally dependent. Lastly, Figure 3b shows an intermediate case.

3.2. Initial Condition

The initial conditions for the model are derived from Van Allen Probes data. MagEIS (Magnetic Electron Ion Spectrometer, Blake et al., 2013) onboard VAP can provide measurements of electron energies from 30 keV up to 4 MeV, however, large uncertainties are associated with energies >1 MeV due to the small geometric factor in its design (Blake et al., 2013). Therefore, only energy channels ranging from ~240 to 904 keV are utilized from MagEIS (energies below 240 keV are irrelevant since E3 channel of the MEPED detector responds to >300 keV). Only two energy channels are of use to us from the REPT (Relativistic Electron-Proton Telescope, Baker et al., 2012) instrument, 1.8 and 2.4 MeV. This is because higher energies typically go undetected in integral energy channels like E3 and P6 due to their substantially lower intensities.

Since the VAP measurements cannot cover low pitch angles near the loss cone, we turned to POES/MetOp to supplement an additional data point around $\alpha_0 \approx 6^\circ$. This additional data point corresponds to the nearest trapped electron measurement in temporal proximity to the initial time, acquired from any of the five POES/MetOp satellites. The initial condition requires differential flux so, only here, we opt to use the MPE data set which has been proton decontaminated and provided as differential flux. The MPE data set is described in detail in Pettit et al. (2021).

To obtain the pitch angle distribution (PAD) for all angles, the VAP's local pitch angle measurements are first mapped to the equator using the TS04 magnetic field model (Tsyganenko & Sitnov, 2005). Zhao et al. (2018)

LI ET AL. 7 of 16

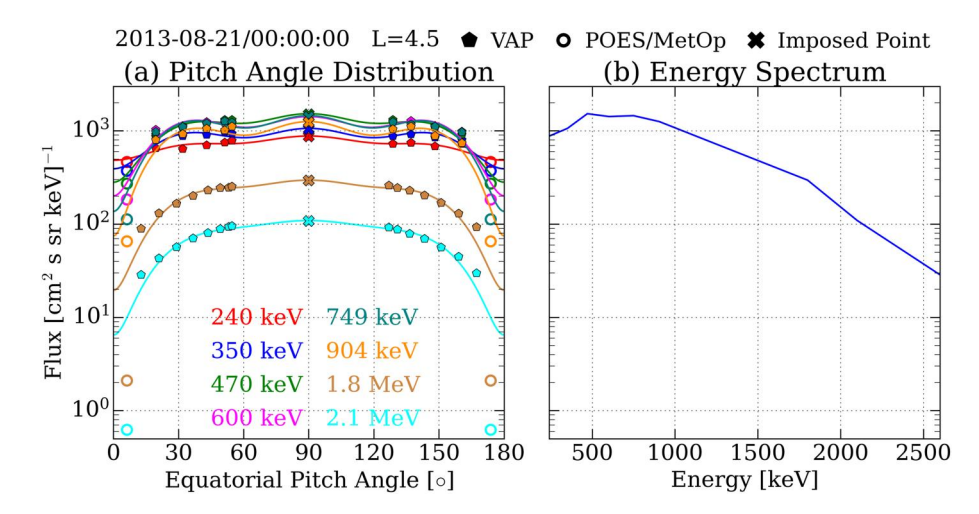


Figure 4. Panel (a) shows the initial PAD for the model obtained from VAP with supplementary points from POES/MetOp at the lowest equatorial pitch angles. An additional point is imposed at $\alpha_0 = 90^{\circ}$ to enforce a flat-top shape. Panel (b) shows the energy spectrum of the initial condition.

found using 6th order even Legendre polynomials to fit energetic electron PADs works well for L > 4, so a similar extrapolation technique is applied here:

$$j_E(\alpha_0) = \sum_{n=0}^{3} c_{2n} P_{2n}(\cos(\alpha_0)), \tag{4}$$

where P_{2n} are the even Legendre Polynomials, and c_{2n} are coefficients to be determined via best fit with data. Note that this is done for each available energy channel and j_F is the PAD for a single energy.

Lastly, during the initial time of this event, VAP was unable to make any measurements near $\alpha_0 = 90^\circ$. Considering that prior to the initial time high equatorial pitch angle measurements from VAP were available and show largely a flat PAD near 90° , we introduce an artificial point at $\alpha_0 = 90^\circ$ with a value 15% larger than the mean of the two closest available measurement to $\alpha_0 = 90^\circ$. In essence, we manually imposed a flat-top distribution for this initial time, as justified by observations. Equation 4 is then used to fit over the VAP pitch angle data, supplementary point provided by POES/MetOp, and the artificially imposed point at $\alpha_0 = 90^\circ$.

Figure 4a depicts the initial PAD obtained at each energy for the electron dropout event. Figure 4b shows the energy spectrum, obtained from the flux values at $\alpha_0 = 90^\circ$, which is the imposed point that is 15% larger in value than the average between the two available measurements closest to $\alpha_0 = 90^\circ$. At lower energies the Legendre polynomials exhibit multiple changes in concavity and is likely an artifact arising from the limited MagEIS data available at high pitch angles. However, this does not pose a problem because our diffusion coefficient efficiently smooths out any gradients at high pitch angles. The energy spectrum in Figure 4b exhibits a phenomenon known as the "bump-on-tail" distribution, which is commonly caused by resonant wave-particle interactions with plasmaspheric hiss waves for lower energy electrons (e.g., Zhao et al., 2019). This initial condition is simulated at a low diffusion case ($D_w = 10^{-9} \, \text{s}^{-1}$) for one drift period to initialize the DLC and BLC electron distribution while largely leaving the initial trapped distribution unmodified. The one-drift-period simulated distribution is then used as the initial condition for the event. The model simulates f which is related to the differential flux by $f = p^2 f$.

3.3. MEPED Energy and Angular Response

The output of our model is the electron phase space density f for a particular L and energy as a function of pitch angle cosine, longitude, and time. To provide constraint from low-altitude electron data obtained from POES/MetOp (e.g., Figures 2b and 2c), the simulated f needs to be converted into count rate. This is achieved by using the MEPED angular response functions (Selesnick et al., 2020) in combination with the previously developed energy response function (Yando et al., 2011). By virtually flying satellites through the simulation, we can

LI ET AL. 8 of 16



replicate the count rates that the detectors would have recorded based on the dynamic state of the electron distribution.

3.4. Parametric Tuning

The two (or six if external source/loss is turned on) free parameters per simulation interval are determined by fitting the simulated count rate to the observed count rate. For reasons detailed in Section 2, a comprehensive longitudinal coverage of the count rate data is required to provide the necessary constraint on the pitch angle diffusion rates, and thus, the time duration of this dropout event is separated into four 3-hr intervals. The parameters are assumed to be constant within each interval, which can be invalid if magnetospheric conditions change rapidly. To mitigate this, the interval boundaries are picked by an orderly distribution of quasi-trapped count rates from the POES/MetOp data such that they tightly follow a general trend (see e.g., Figures 6–8 in Selesnick et al., 2020).

The parameters are iteratively tuned to minimize the metric:

$$K^{2} = \sum_{i}^{N} \left[\log_{10}(d_{i}) - \log_{10}(p_{i}) \right]^{2},$$
 (5)

where, N is the total number of data points, d_i are the observed count rates, and p_i are the simulated count rates. The Quasi-Newton method is used to iteratively find the set of parameters which achieves the minimum K^2 starting from an initial set of seed parameters (Tarantola, 2005, p. 79). Constant background rates are estimated for each channel and is determined by the count rate floor reached by the 0° telescope during quiet times (excluding a few outliers which occasionally fall below). Count rates below the background rate are included in the model but excluded from the fit. Lastly, temporal continuity in the model is achieved by using the evolved f of a previous interval as the initial condition for the next interval, where the parameters are again obtained by recursive fit.

4. August 2013 Dropout Event

A rapid electron dropout was observed by VAP across a broad range of energies at L=4.5 on 21st August 2013. Figure 5a shows the SYM-H index variation during this event, which attains a minimum of -37 nT. Despite this being a small storm, it has triggered a significant response in the radiation belt. Figure 5c shows 909 keV electron flux measurements from the MagEIS 90° local pitch angle bin along the VAP orbits. To better illustrate the flux drop, Figure 5d shows the 90° observations interpolated to L=4.5, for three selected energies, where the fluxes all decrease by approximately half an order of magnitude. The precise timing of this dropout is not well resolved, but it is evident that the dropout occurs within \sim 76 min, between the two inbound passes of VAP A & B just prior to 04 hr UT. Figure 5b shows that the dayside magnetopause location predicted by the Shue et al. (1998) model stays above eight Earth radii, and the last closed drift shell (LCDS) computed traditionally by field-line tracing (see e.g., Huang et al., 2023) remains near $L^* \sim 7$ during the entirety of the event. This suggests that the dropout is likely driven by precipitation resulting from pitch angle diffusion rather than magnetopause shadowing loss in combination with radial diffusion.

In this work, we are primarily interested in what happens during the dropout, so our simulation covers the quiet time just shortly before the dropout and continues until just before fluxes begin recovering to their pre-storm levels. The simulated time range for this event is from 00 to 12 hr UT on 21st August 2013. Between approximately 04 and 12 hr UT, the electron flux at L = 4.5 remain in a depleted state for a broad range of energies and there appears to be no obvious energy dependence in this dropout. This 12-hr simulation time domain is divided into four equal 3-hr intervals as marked by the colored bars above Figure 5a. Interval 1 (red) will quantify model parameters during a quiet time state of the radiation belts, while intervals 2, 3, and 4 will quantify storm-time conditions.

This dropout event is chosen for the study since it is a small storm during which the adiabatic effects on electron flux is insignificant. Selesnick (2006) showed based on model results, that adiabatic effects were small for low-altitude electrons for two intense storms (SYM-H \sim -200 nT) at L=3.5. Despite our event occurring at a higher L=4.5, the storm magnitude is notably smaller (SYM-H = -37 nT). Additionally, Selesnick (2006) showed that

LI ET AL. 9 of 16

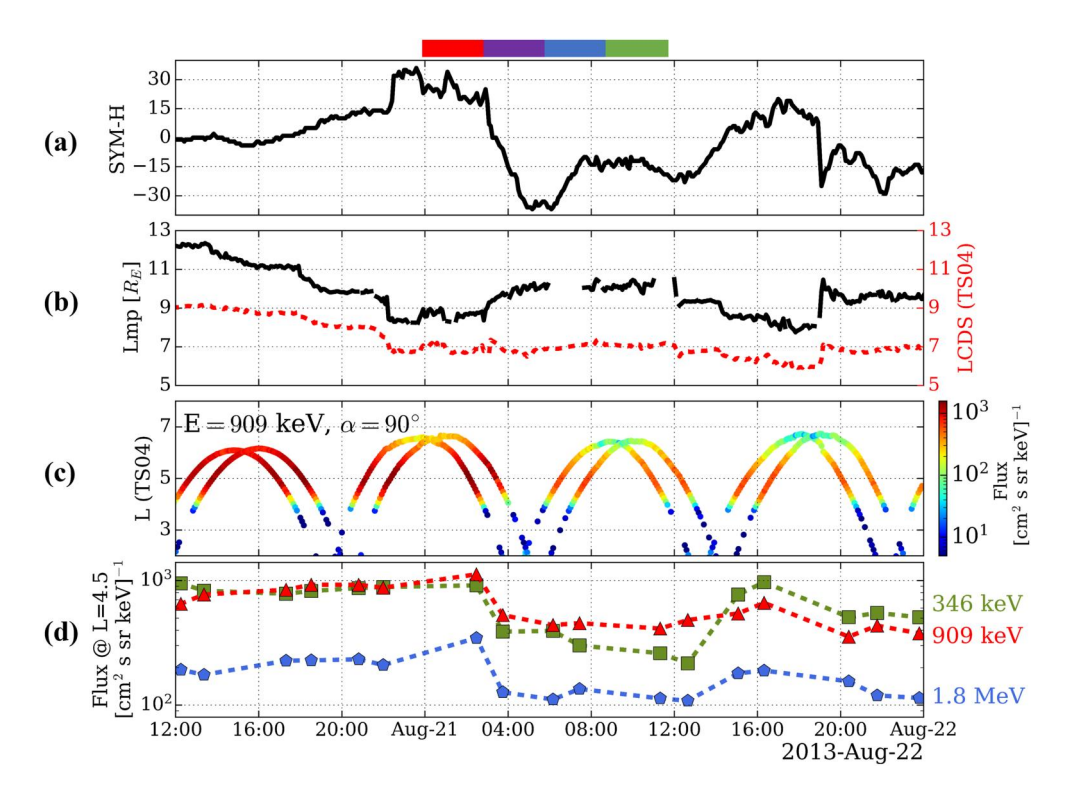


Figure 5. Panel (a) shows the SYM-H and solar wind pressure variation during the event. Panel (b) shows the predicted dayside magnetopause location and the last closed drift shell (LCDS). Panel (c) shows the flux measurement for a selected energy and local pitch angle as measured by the VAPs along their orbit trajectory, and (d) shows the flux variation taken at only L = 4.5 for a few selected energies. The colored bars on top of panel (a) correspond to the interval periods of the four 3-hr intervals, starting at 00, 03, 06, 09 UT of 21st August 2013.

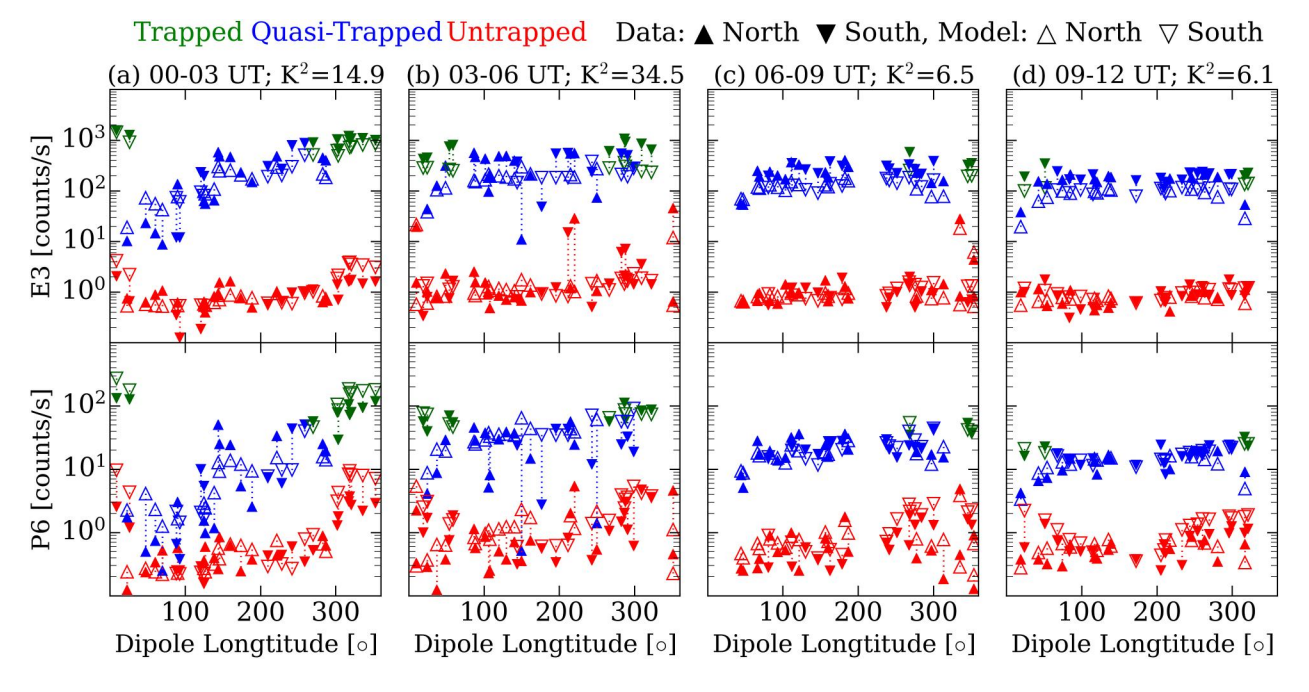


Figure 6. Electron count rate data (solid triangles) from five POES/MetOp satellites interpolated at L = 4.5 on 21st August 2013. Model count rate (hollow triangles) is shown with dashed lines connecting each simulated count rate to its corresponding data point. Column (a) is taken during a 3-hr quiet pre-storm interval. Column (b) is during the initial storm main phase. Columns (c) and (d) are the subsequent hours during the main phase. The goodness of fit per each interval is provided in the title of each column.

LI ET AL. 10 of 16

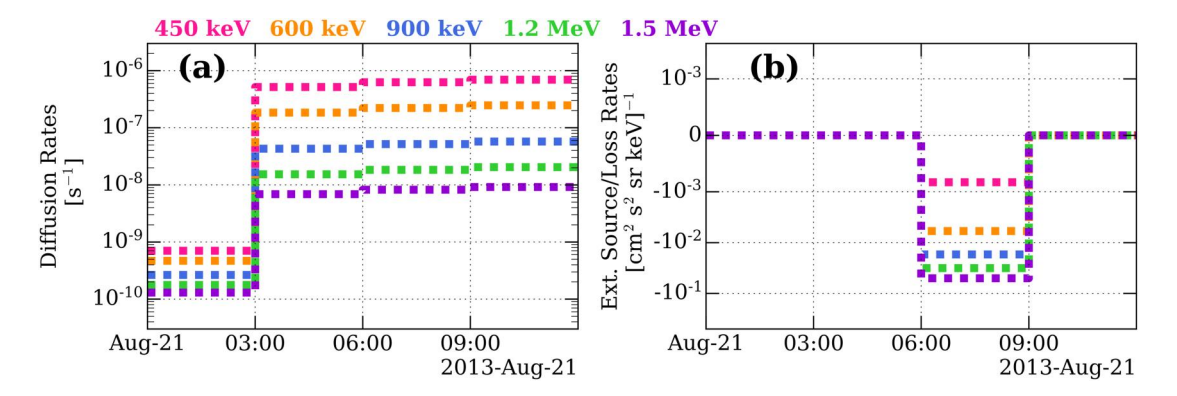


Figure 7. Evolution of the model parameters over the four 3-hr intervals for select energies. Panel (a) shows the pitch angle diffusion rates $(D_w \tilde{E}^{-\mu})$ and panel (b) shows the source and loss rates $\left(S_0 \tilde{E}^{-\nu} - L_0 \tilde{E}^{-\eta}\right)$ which are only non-zero during the third interval. Linear threshold for the symmetric logarithmic y-axes is set at 10^{-3} .

the most significant changes due to adiabatic effects for low-altitude electrons is their mirror point altitude, which can be quickly compensated by even moderate rates of pitch angle diffusion.

5. Model Results

Solid markers in Figure 6 show the observed count rates as a function of longitude during this event taken from the E3 and P6 channels for each of the four 3-hr intervals. Plotted on top with hollow points are the simulated count rates obtained by flying virtual satellites through the model. Both the model and data have been categorized based on their measurement taken outside of the DLC (trapped in green), within the DLC (quasi-trapped in blue) and within the BLC (untrapped in red) and the hemisphere which the measurement was taken at (upward vs. downward triangles). The four columns all together depict the temporal evolution of the observed and modeled electron dynamics for this event.

Figure 6a depicts the quiet time 3-hr interval before the storm main phase. The quasi-trapped count rate data increased with longitude, indicating a slow rate of pitch angle diffusion, and was successfully captured by the model. However, our model slightly overestimates trapped count rates in the P6 channel during this interval for several possible reasons. First, the diffusion coefficient's functional form (Equation 3), derived via observations at a different time, may not accurately represent the diffusion coefficient during the initial interval. Second, P6 is more sensitive to >1 MeV electrons than E3, leading to greater manifestations of uncertainties associated with interpolating the initial energy spectrum across the 1–1.8 MeV gap (as detailed in Section 3.2). Third, cross-calibration between POES/MetOp and VAP is likely required for the initial condition but is not performed for this work. Finally, the lone data point from POES/MetOp at low pitch angles, especially at higher energies, for the initial condition was not captured by the fit (see Figure 4a). These inaccuracies during this interval are associated with higher order effects which are inconsequential and decay rapidly in later intervals when the diffusion rate

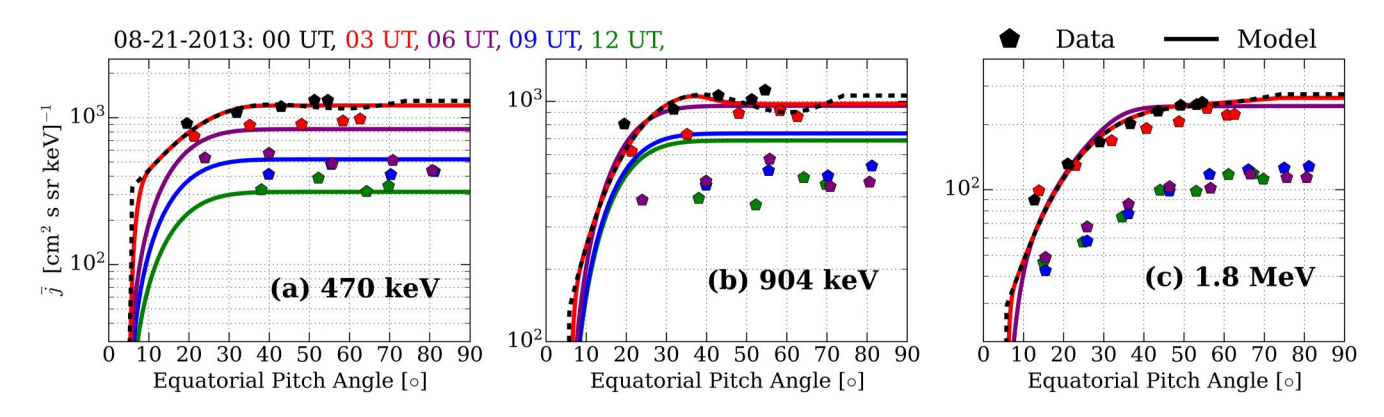


Figure 8. Drift averaged model solutions (lines) compared with VAP observations (pentagons) at L = 4.5 for different intervals (in different colors) for select energies. High-altitude data on panels (a) and (b) are taken from the MagEIS instrument, while panel (c) is from REPT. Dashed line corresponds to the model's initial condition.

LI ET AL. 11 of 16



increases. This is supported by the following interval (Figure 6b) when trapped count rates in P6 become reasonably well matched.

Figure 6b shows simulated and observed count rates for the second interval during the storm's initial main phase. The SYM-H index drops quickly during this interval, and the rapid changes in magnetospheric conditions could violate the constant parameter assumption imposed on our model. The scattered count rates in the quasi-trapped population show further indications of such violation. Despite that, the model still reproduced a substantial portion of the observed electron distribution, implying that the assumption of constant parameters is only weakly violated, and its impact remains minor. The scatter explains the relatively higher K^2 during this interval (provided in the title of each column in Figure 6). Furthermore, during this interval, the flat distribution exhibited by the quasi-trapped population indicates fast pitch angle diffusion which is reflected in both the model count rate, and the estimated rates of pitch angle diffusion (shown in Figure 7a). Figure 7a shows an increase in pitch angle diffusion for all energies by 2–3 orders of magnitude for all energies. Since the main trend of the data distribution is largely replicated by the model during the first two intervals, the external source/loss factor remains off up to the end of the second interval.

Figure 6c shows the model and observed count rates for the third interval. Here, the external source/loss function was enabled, because without it, the simulated trapped and untrapped count rates in the P6 channel were uniformly overestimated by nearly an order of magnitude (not shown). Energy dependence of pitch angle diffusion can be identified in the data where the quasi-trapped count rate distribution is flatter as a function of longitude in the lower energy channel, E3, than the higher energy channel, P6. This feature was recognized by the model and higher pitch angle diffusion rates were obtained at lower energies, similar to the previous interval, as shown in Figure 7a. The energy dependance of the external loss during this interval is shown in Figure 7b, which indicates faster external loss at higher energies. For electron energies <450 keV, the rates of external source/loss are negligible. This plays an important role in decreasing the energetic trapped and quasi-trapped electron count rates in the P6 channel without scattering electrons into the BLC, as required by the data.

Figure 6d depicts the final storm-time interval, and the data are again well reproduced by the model. The pitch angle diffusion rates determined by the model, Figure 7a, continues to show higher rates at lower energy, and remains significantly faster than in quiet times. This energy dependence is again evident in the data illustrated by the flatter quasi-trapped count slope in longitude in the E3 channel. No external source/loss was required during this interval, and it was therefore turned off.

Notably, slight under prediction of the simulated count rates is present across all intervals compared to observed E3 count rates, however, this discrepancy is not significant enough to warrant the introduction of external source/loss mechanisms. Finally, the reasonable match between the model and observed trapped count rates for all four intervals, in both E3 and P6, shows that the model has successfully captured the electron flux decrease throughout the event.

6. Comparison With High-Altitude Data

The successful reproduction of low-altitude electron distributions made by the model may not imply the same for high altitudes. The model's initial conditions were derived mainly using high-altitude data from VAP, but its evolution was exclusively guided by the low-altitude electron distribution. This raises the question: can a model constrained by low-altitude data effectively replicate the changes at higher altitudes?

Figure 8 answers this question, shown with VAP data taken at the end times of each 3-hr interval (in pentagon symbols). The model solutions at the end of each interval are shown by the colored solid curves, while the initial condition is reiterated by the black dashed line. The best fits with low-altitude data, as quantified by K^2 , occurred in intervals 3 and 4. Correspondingly, Figures 8a and 8b show the best agreement between observations and the model at 09 UT (blue) and 12 UT (green), the end times of the 3rd and 4th interval, for electron energies below 1 MeV. Interval 2 at low altitudes showed the worst fit between the model and observed count rates which is likely due to the weak violation of the constant parameters assumption. As a result, the match between model and observations during this interval (in purple) is the poorest at high altitudes as demonstrated in Figures 8a and 8b. These transient dynamics are challenging for the model to fully capture. For this interval, our quantifications of the model parameters can be interpreted as a 3-hr average.

LI ET AL. 12 of 16

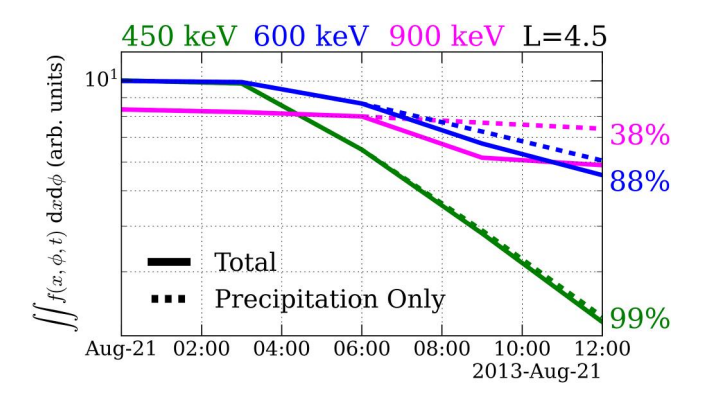


Figure 9. The variation of total flux (presented in arbitrary units) in the system for each energy as a function of time. The percentages on the right represent the change in flux due to precipitation only.

Figure 8c compares model results with VAP observation for 1.8 MeV electrons. Notably, the model predicts a complete extinction of electrons in the 3rd and 4th intervals (thus not appearing in Figure 8c), contradicting observations. This discrepancy is attributed to the limited constraint at relativistic energies provided by the POES/MetOp data. Both E3 and P6 are integral energy channels responding primarily to the sub-1 MeV population and their sensitivity to higher energy electrons is limited by the more abundant population at lower energy. The slight over prediction of the model compared to VAP observations for 904 keV (Figure 8b) is likely due to the same reason.

The model was successful in reproducing low-altitude electron distributions as observed by POES/MetOp. Further comparisons with high-altitude data observed by VAP exclusively reveal the discrepancies at relativistic energies. Nonetheless, our model agreed reasonably well at low and high altitudes for energies below ~1 MeV, and hence, in this range, we can conclude that the parameters quantified by our model are representative of actual magnetospheric conditions.

Having established the model's domain of validity, we can now address our primary question: what is the contribution of precipitation to the observed electron dropout during this event? The change in total flux within the system (integrated over x or α_0 and ϕ) can be attributed either to atmospheric loss (precipitation) or to external source/loss mechanisms. Therefore, to isolate the loss due to precipitation, the total contribution of the external source/loss (Equation 2) is determined and then removed from the total flux to obtain the flux loss due to precipitation only. Figure 9 depicts the variation in total flux within the system in comparison to the variation of flux due to precipitation alone. The contribution of precipitation to the electron dropout progressively decreases with energy; it is \sim 99% at 450 keV, 88% at 600 keV, and 38% at 900 keV. This suggests that for energies below \sim 850 keV precipitation is the dominant cause for the observed rapid electron dropout, while another mechanism is the primary cause at higher energy.

7. Discussion and Conclusions

In this study, we used a drift-diffusion model, that includes azimuthal drift, pitch angle diffusion and atmospheric backscatter, to simulate a rapid electron dropout event at L=4.5 on 21st August 2013. Additionally, we used angular and energy response functions for the MEPED detector onboard POES/MetOp to accurately simulate electron data for comparison with observed count rates (Selesnick et al., 2020; Yando et al., 2011). Low-altitude data obtained from a constellation of five POES/MetOp satellites is used to constrain the evolution of the electron distribution and pitch angle diffusion rates during this event and the contribution of precipitation to the total loss is determined. We found that during storm-time, pitch angle diffusion was significantly faster for lower electrons energies. Additional, or external, loss effects were introduced, which were significant especially at higher energy from 06 to 09 UT, since without it, low-altitude electron data could not be reproduced by the model from pitch angle diffusion alone. Ultimately, the model determined that precipitation contributed 99% to the total observed loss of 450 keV electrons, as observed from high altitudes, 88% for 600 keV, and 38% for 900 keV, so that precipitation was the dominant loss mechanism for electron energies below \sim 850 keV. For the electron population with energies exceeding \sim 1 MeV, the E3 and P6 data provided insufficient constraint, resulting in discrepancies between the model and observed high-altitude data.

The energy dependence and the rate of pitch angle diffusion as quantified by the model appears to be consistent with plasmaspheric hiss waves (e.g., Ni et al., 2014) which could serve as the underlying mechanism responsible for the precipitation loss. Statistical studies show that plasmaspheric hiss waves are often observed within and near the plasmapause location (see e.g., Thorne, 2010 and references therein). An empirical plasmapause model (Liu et al., 2015) shows that, during this event, the plasmapause partially encloses the L=4.5 region, favoring the plasmaspheric hiss interpretation. Further, VAP-B observed broadband hiss waves at the start of \sim 04 UT persisting until \sim 10 UT (not shown), which is reasonably in line with the increasing rates of pitch angle diffusion quantified by our model. Chorus waves can also share a similar energy dependence and scattering rate with plasmaspheric hiss and could serve as another possible mechanism for rapid pitch angle scattering of low energy electrons (e.g., W. Li et al., 2014). Other contenders such as electromagnetic ion cyclotron waves are generally

LI ET AL. 13 of 16



efficient at scattering electrons at highly relativistic energies, which is inconsistent with our model predictions (e.g., Millan et al., 2007; Miyoshi et al., 2008). However, the modeling approach used in this work has quantified pitch angle diffusion rates without relying on accurate wave measurements.

External loss rates determined by the model showed faster loss for higher energy. While the precise mechanism is not specified in the model, the energy dependance as quantified by the model is consistent with loss due to magnetopause shadowing in combination with outward radial diffusion (see e.g., Fei et al., 2006; Tu et al., 2019). This is because faster drift speeds associated with higher energy particles experience magnetopause shadowing effects more quickly per unit time, and as a result, the inward propagation of the loss becomes positively energy dependent (Olifer et al., 2021).

While the model provides good agreement with low-altitude data and moderate agreement with high-altitude data, there are several areas of possible improvement. As discussed in Section 6, the energy constraint provided by E3 and P6 are insufficiently sensitive to highly relativistic electrons. Additionally, the energy dependence of the diffusion coefficient, external source/loss, and atmospheric backscatter ratio (F_b) were crudely modeled. Here, we use a reasonable approximation to backscatter given that we also approximate the loss cone distribution with a bounce-averaged model. To correctly model the loss cone distribution and their interactions with the atmosphere would require a more sophisticated Monte-Carlo approach and a non-bounce averaged model, as done in Selesnick et al. (2004). Nonetheless, this was not performed here as it adds significant complexity to the model.

Although our simulation focused on a single dropout event, we have demonstrated the effectiveness of a datadrive model for estimating pitch angle diffusion rates without the need for plasma wave measurements. Further model improvements could be made by the inclusion of other low-altitude satellites to improve longitudinal coverage and model cadence. The inclusion of high-altitude data from multiple satellites, as that used for the initial condition, could provide more comprehensive constraints on the model across all pitch angles. However, the model already has distinguished precipitation loss from the total loss observed during an electron dropout event, addressing an unresolved question in radiation belt dynamics.

Data Availability Statement

POES and MetOp SEM-2 data used in this study are available online (https://www.ncei.noaa.gov/products/poes-space-environment-monitor). Van Allen Probes MagEIS and REPT data are available online (https://spdf.gsfc.nasa.gov/pub/data/rbsp/rbspa/l3/ect/). NASA's OMNIWeb data is available at (https://omniweb.gsfc.nasa.gov/). The model results of the electron distribution functions per each simulation interval, as well as the MPE data set files used specifically in this study are also available online publicly (https://doi.org/10.5281/zenodo.10694739). The quantified model parameters can be found on Table S1.

Acknowledgments

This work was supported by the NASA Grants 80NSSC19M0146, 80NSSC21K1312, and 80NSSC21K2008, DOE Grant DE-SC0020294, and NSF Grant AGS 1752736. Z.-G. Li would like to thank Prof. Hong Zhao for the thoughtful discussion regarding geometric factor differences between MagEIS' highenergy unit and REPT. Z.-G. Li would also thank Dr. Joshua Pettit for his assistance in working with the MPE data set.

References

- Abel, B., & Thorne, R. M. (1999). Modeling energetic electron precipitation near the South Atlantic anomaly. *Journal of Geophysical Research*, 104(A4), 7037–7044. https://doi.org/10.1029/1999JA900023
- Baker, D. N. (2000). The occurrence of operational anomalies in spacecraft and their relationship to space weather. *IEEE Transactions on Plasma Science*, 28(6), 2007–2016. https://doi.org/10.1109/27.902228
- Baker, D. N., Jaynes, A. N., Kanekal, S. G., Foster, J. C., Erickson, P. J., Fennell, J. F., et al. (2016). Highly relativistic radiation belt electron acceleration, transport, and loss: Large solar storm events of March and June 2015. *Journal of Geophysical Research: Space Physics*, 121(7), 6647–6660. https://doi.org/10.1002/2016JA022502
- Baker, D. N., Kanekal, S. G., Hoxie, V. C., Batiste, S., Bolton, M., Li, X., et al. (2012). The relativistic electron-proton telescope (REPT) instrument on board the radiation belt storm probes (RBSP) spacecraft: Characterization of Earth's radiation belt high-energy particle populations. *Space Science Reviews*, 179(1–4), 337–381. https://doi.org/10.1007/s11214-012-9950-9
- Barker, A. B., Li, X., & Selesnick, R. S. (2005). Modeling the radiation belt electrons with radial diffusion driven by the solar wind. *Space Weather*, 3(10), S10003. https://doi.org/10.1029/2004SW000118
- Blake, J. B., Carranza, P. A., Claudepierre, S. G., Clemmons, J. H., Crain, W. R., Dotan, Y., et al. (2013). The magnetic electron ion spectrometer (MagEIS) instruments aboard the radiation belt storm probes (RBSP) spacecraft. *Space Science Reviews*, 179(1–4), 383–421. https://doi.org/10.1007/s11214-013-9991-8
- Davidson, G. T. (1976). An improved empirical description of the bounce motion of trapped particles. *Journal of Geophysical Research*, 81(22), 4029–4030. https://doi.org/10.1029/JA081i022p04029
- Evans, D. S., & Greer, M. S. (2000). Polar orbiting environmental satellite space environmental monitor—2: Instrument descriptions and archive data documentation. National Oceanic and Atmospheric Administration, Space Environment Centre.
- Fei, Y., Chan, A. A., Elkington, S. R., & Wiltberger, M. J. (2006). Radial diffusion and MHD particle simulations of relativistic electron transport by ULF waves in the September 1998 storm. *Journal of Geophysical Research*, 111(A12), A12209. https://doi.org/10.1029/2005JA011211 Finlay, C. C., Maus, S., Beggan, C. D., Bondar, T. N., Chambodut, T. A., Chernova, T. A., et al. (2010). International geomagnetic reference field: The eleventh generation. *Geophysical Journal International*, 183(3), 1216–1230. https://doi.org/10.1111/j/1365-246X.2010.04804.x

LI ET AL. 14 of 16



- Fytterer, T., Mlynczak, M. G., Nieder, H., Pérot, K., Sinnhuber, M., Stiller, G., & Urban, J. (2015). Energetic particle induced intra-seasonal variability of ozone inside the Antarctic polar vortex observed in satellite data. *Atmospheric Chemistry and Physics*, 15(6), 3327–3338. https://doi.org/10.5194/acp-15-3327-2015
- Ganushkina, N. Y., Dandouras, I., Shprits, Y. Y., & Cao, J. (2011). Locations of boundaries of outer and inner radiation belts as observed by cluster and double star. *Journal of Geophysical Research*, 116(A9), A09234. https://doi.org/10.1029/2010JA016376
- Green, J. C. (2013). MEPED telescope data processing algorithm theoretical basis document. National Oceanic and Atmospheric Administration, National Geophysical Data Center.
- Huang, J., Lyu, X., Tu, W., Albert, J. M., & Lee, S.-Y. (2023). Modeling the effects of drift orbit bifurcation on the magnetopause shadowing loss of radiation belt electrons. *Geophysical Research Letters*, 50(24), e2023GL106359. https://doi.org/10.1029/2023GL106359
- Imhof, W. L. (1968). Electron precipitation in the radiation belts. Journal of Geophysical Research, 73(13), 4167–4184. https://doi.org/10.1029/ JA073i013n04167
- Kennel, C. F., & Petschek, H. E. (1966). Limits on stably trapped particle fluxes. *Journal of Geophysical Research*, 71, 1–28. https://doi.org/10.1177/1069072705283987
- Li, W., Thorne, R. M., Ma, Q., Ni, B., Bortnik, J., Baker, D. N., et al. (2014). Radiation belt electron acceleration by chorus waves during the 17 March 2013 storm. *Journal of Geophysical Research: Space Physics*, 119(6), 4681–4693. https://doi.org/10.1002/2014JA019945
- Li, X., Baker, D. N., Temerin, M., Cayton, T. E., Reeves, E. G. D., Christensen, R. A., et al. (1997). Multisatellite observations of the outer zone electron variation during the November 3–4, 1993, magnetic storm. *Journal of Geophysical Research*, 102(A7), 14123–14140. https://doi.org/10.1029/97IA01101
- Liu, X., Liu, W., Cao, J. B., Fu, H. S., Yu, J., & Li, X. (2015). Dynamic plasmapause model based on THEMIS measurements. Journal of Geophysical Research: Space Physics, 120(12), 10543–10556. https://doi.org/10.1002/2015JA021801
- Lyons, L. R., Thorne, R. M., & Kennel, C. F. (1972). Pitch-angle diffusion of radiation belt electrons within the plasmasphere. *Journal of Geophysical Research*, 77(19), 3455–3474. https://doi.org/10.1029/JA077i019p03455
- McIlwain, C. E. (1961). Coordinates for mapping the distribution of magnetically trapped particles. *Journal of Geophysical Research*, 66(11), 3681–3691. https://doi.org/10.1029/JZ066i011p03681
- Meraner, K., & Schmidt, H. (2018). Climate impact of idealized winter polar mesospheric and stratospheric ozone losses as caused by energetic particle precipitation. *Atmospheric Chemistry and Physics*, 18(2), 1079–1089, https://doi.org/10.5194/acp-18-1079-2018
- Millan, R. M., Lin, R. P., Smith, D. M., & McCarthy, M. P. (2007). Observation of relativistic electron precipitation during a rapid decrease of trapped relativistic electron flux. *Geophysical Research Letters*, 34(10), L10101. https://doi.org/10.1029/2006GL028653
- Millan, R. M., Yando, K. B., Green, J. C., & Ukhorskiy, A. Y. (2010). Spatial distribution of relativistic electron precipitation during a radiation belt depletion event. *Geophysical Research Letters*, 37(20), L20103. https://doi.org/10.1029/2010GL044919
- Miyoshi, Y., Sakaguchi, K., Shiokawa, K., Evans, D., Albert, J., Connors, M., & Jordanova, V. (2008). Precipitation of radiation belt electrons by EMIC waves, observed from ground and space. *Geophysical Research Letters*, 35(23), L23101. https://doi.org/10.1029/2008GL035727
- Ni, B., Li, W., Thorne, R. M., Bortnik, J., Ma, Q., Chen, L., et al. (2014). Resonant scattering of energetic electrons by unusual low-frequency hiss.
- Geophysical Research Letters, 41(6), 1854–1861. https://doi.org/10.1002/2014GL059389

 Olifer, L., Mann, I. R., Ozeke, L. G., Claudepierre, S. G., Baker, D. N., & Spence, H. E. (2021). On the similarity and repeatability of fast radiation belt loss: Role of the last closed drift shell. Journal of Geophysical Research: Space Physics, 126(11), e2021JA029957. https://doi.org/10.1029/
- Pettit, J. M., Randall, C. E., Peck, E. D., & Harvey, V. L. (2021). A new MEPED-based precipitating electron data set. *Journal of Geophysical Research: Space Physics*, 126(12), e2021JA029667. https://doi.org/10.1029/2021JA029667
- Pham, K. H., Tu, W., & Xiang, Z. (2017). Quantifying the precipitation loss of radiation belt electrons during a rapid dropout event. *Journal of Geophysical Research: Space Physics*, 122(10), 10287–10303. https://doi.org/10.1002/2017ja024519
- Press, W. H., Teukolsky, S. A., Vetterling, W. T., & Flannery, B. P. (2007). Numerical recipes 3rd edition: The art of scientific computing. Cambridge University Press.
- Robinson, R. M., Vondrak, R. R., Miller, K., Dabbs, T., & Hardy, D. (1987). On calculating ionospheric conductances from the flux and energy of precipitating electrons. *Journal of Geophysical Research*, 92(A3), 2565–2569. https://doi.org/10.1029/JA092iA03p02565
- Roederer, J. G. (1970). Dynamics of geomagnetically trapped radiation. Springer.
- Schulz, M., & Lanzerotti, L. J. (1974). Particle diffusion in the radiation belts. In Physics and chemistry in space (Vol. 7). Springer.
- Selesnick, R. (2006). Source and loss rates of radiation belt relativistic electrons during magnetic storms. *Journal of Geophysical Research*, 111(A4), A04210. https://doi.org/10.1029/2005JA011473
- Selesnick, R. S., Blake, J. B., & Mewaldt, R. A. (2003). Atmospheric losses of radiation belt electrons. *Journal of Geophysical Research*, 108(A12), 1468. https://doi.org/10.1029/2003JA010160
- Selesnick, R. S., Looper, M., & Albert, J. (2004). Low-altitude distribution of radiation belt electrons. *Journal of Geophysical Research*, 109(A11), A11209. https://doi.org/10.1029/2004ja010611
- Selesnick, R. S., Tu, W., Yando, K. B., Millan, R. M., & Redmon, R. J. (2020). POES/MEPED angular response functions and the precipitating radiation belt electron flux. Journal of Geophysical Research: Space Physics, 125(9), e2020JA028240. https://doi.org/10.1029/2020JA028240
- Shprits, Y., Daae, M., & Ni, B. (2012). Statistical analysis of phase space density buildups and dropouts. *Journal of Geophysical Research*, 117(A1), A01219. https://doi.org/10.1029/2011JA016939
- Shprits, Y. Y., Li, W., & Thorne, R. M. (2006). Controlling effect of the pitch angle scattering rates near the edge of the loss cone on electron lifetimes. *Journal of Geophysical Research*, 111(A12), A12206. https://doi.org/10.1029/2006JA011758
- Shprits, Y. Y., Thorne, R. M., Friedel, R., Reeves, G. D., Fennell, J., Baker, D. N., & Kanekal, S. G. (2006). Outward radial diffusion driven by losses at magnetopause. *Journal of Geophysical Research*, 111(A11), 11214. https://doi.org/10.1029/2006JA011657
- Shprits, Y. Y., Thorne, R. M., Reeves, G. D., & Friedel, R. (2005). Radial diffusion modeling with empirical lifetimes: Comparison with CRRES observations. *Annales de Geophysique*, 23(4), 1467–1471. https://doi.org/10.5194/angeo-23-1467-2005
- Shue, J. H., Song, P., Russell, C. T., Steinberg, J. T., Chao, J. K., Zastenker, G., et al. (1998). Magnetopause location under extreme solar wind conditions. *Journal of Geophysical Research*, 103(A8), 17691–17700. https://doi.org/10.1029/98JA01103
- Tarantola, A. (2005). Inverse problem theory and methods for model parameter estimation. Society for Industrial and Applied Mathematics. https://doi.org/10.1137/1.9780898717921
- Thorne, R. M. (2010). Radiation belt dynamics: The importance of wave-particle interactions. *Geophysical Research Letters*, 37(22), L22107. https://doi.org/10.1029/2010GL044990
- Thorne, R. M., & Kennel, C. F. (1971). Relativistic electron precipitation during magnetic storm main phase. *Journal of Geophysical Research*, 76(19), 4446–4453. https://doi.org/10.1029/JA076i019p04446

LI ET AL. 15 of 16



- Tsyganenko, N. A., & Sitnov, M. I. (2005). Modeling the dynamics of the inner magnetosphere during strong geomagnetic storms. *Journal of Geophysical Research*, 110(A3), A03208. https://doi.org/10.1029/2004ja010798
- Tu, W., Selesnick, R., Li, X., & Looper, M. (2010). Quantification of the precipitation loss of radiation belt electrons observed by SAMPEX. Journal of Geophysical Research, 115(A7), A07210. https://doi.org/10.1029/2009JA014949
- Tu, W., Xiang, Z., & Morley, S. K. (2019). Modeling the magnetopause shadowing loss during the June 2015 dropout event. Geophysical Research Letters, 46(16), 9388–9396. https://doi.org/10.1029/2019GL084419
- Turner, D. L., Angelopoulos, V., Morley, S. K., Henderson, M. G., Reeves, G. D., Li, W., et al. (2014). On the cause and extent of outer radiation belt losses during the 30 September 2012 dropout event. *Journal of Geophysical Research: Space Physics*, 119(3), 1530–1540. https://doi.org/10.1002/2013JA019446
- Turner, D. L., Shprits, Y., Hartinger, M., & Angelopoulos, V. (2012). Explaining sudden losses of outer radiation belt electrons during geomagnetic storms. *Nature Physics*, 8(3), 208–212. https://doi.org/10.1038/nphys2185
- Van Allen, J. A., Ludwig, G. H., Ray, E. C., & McIlwain, C. E. (1958). Observation of high intensity radiation by satellites 1958 Alpha and Gamma. *Journal of Jet Propulsion*, 28(9), 588–592. https://doi.org/10.2514/8.7396
- Yando, K., Millan, R. M., Green, J. C., & Evans, D. S. (2011). A Monte Carlo simulation of the NOAA POES medium energy proton and electron detector instrument. *Journal of Geophysical Research*, 116(A10), A10231. https://doi.org/10.1029/2011JA016671
- Yu, Y., Jordanova, V. K., McGranaghan, R. M., & Solomon, S. C. (2018). Self-consistent modeling of electron precipitation and responses in the ionosphere: Application to low-altitude energization during substorms. Geophysical Research Letters, 45(13), 6371–6381. https://doi.org/10. 1029/2018g1078828
- Zhao, H., Friedel, R. H. W., Chen, Y., Reeves, G. D., Baker, D. N., Li, X., et al. (2018). An empirical model of radiation belt electron pitch angle distributions based on Van Allen Probes measurements. *Journal of Geophysical Research: Space Physics*, 123(5), 3493–3511. https://doi.org/ 10.1029/2018JA025277
- Zhao, H., Ni, B., Li, X., Baker, D. N., Johnston, W. R., Zhang, W., et al. (2019). Plasmaspheric hiss waves generate a reversed energy spectrum of radiation belt electrons. *Nature Physics*, 15(4), 367–372. https://doi.org/10.1038/s41567-018-0391-6

LI ET AL. 16 of 16